

# Geomorphology of lunar grabens requires igneous dikes at depth

Christian Klimczak<sup>1,2</sup>

<sup>1</sup>Department of Terrestrial Magnetism, Carnegie Institution of Washington, 5241 Broad Branch Road NW, Washington, D.C. 20015, USA

<sup>2</sup>Department of Geology, University of Georgia, GG Building, 210 Field Street, Athens, Georgia 30602, USA

## ABSTRACT

Dense coverage of high-resolution topographic measurements from the Lunar Orbiter Laser Altimeter (LOLA) now allows for a global survey of the long-wavelength morphology of lunar grabens, with important implications for the geologic processes that form them. Comparing model ground displacements for grabens that arise solely from faulting, and from faulting involving a dike at depth, with topographic measurements across some of the most prominent and best-preserved grabens shows that many of them are underlain by a dike. Matching ground displacement models to topographic observations is the only way to detect, and also provide specific geometric information about, dikes too small to be resolved in available gravity and magnetic measurements, and thus allows for quantitative assessments of magma source depths and required magma overpressures. Dike-forming magmas are likely mantle derived, originating from depths greater than 20 km, with dike widths exceeding 100–500 m. Such dike geometric properties are only plausible if a mechanically weak lunar lithosphere was under extension at the time of dike emplacement.

## INTRODUCTION

Planets without major erosional processes can retain the morphologic expressions of tectonic structures over geologic time scales. This allows faults to be analyzed in terms of their dips and offsets, the depth extent to which the faults deformed their host rocks, and the ground displacements resultant from all slip events over the lifetime of faulting. In particular, the structural traits of a planetary graben—a linear topographic low caused by the down-dropping of a crustal block along two bounding, antithetic normal faults—include a gentle synclinal flexure in the rock units below the fault planes (foot-wall syncline) and a gentle anticlinal flexure in the rock units above the fault planes (hanging wall anticline) (Schultz et al., 2010). The vertical offsets of these faults are readily measurable as the topographic differences between the top and bottom of the two fault scarps (see Fig. DR1 in the GSA Data Repository<sup>1</sup>).

## LUNAR GRABEN GEOMORPHOLOGY

After 5 yr of orbital operations, the coverage of topographic measurements with the Lunar Orbiter Laser Altimeter (LOLA) (Smith et al., 2010) aboard the Lunar Reconnaissance Orbiter (LRO) now allows for an in-depth morphologic analysis of lunar grabens. They occur peripheral to some near-side mare units (Waters and Johnson, 2010), within floor-fractured craters (Schultz, 1976), and inside larger impact structures, such as the Schrödinger basin (Wilhelms et al., 1979). The complex graben pat-

tern within Schrödinger consists of large and small structures together broadly defining basin-radial and basin-concentric orientations (Fig. 1A). Four topographic profiles across grabens obtained from a gridded LOLA elevation model (Fig. 1B) show that these structures are located central to a 100–200-m-high topographic rise (Fig. 2). Altimetry indicates that the grabens are 2–3 km in width and 200–300 m deep. Similarly, LOLA data across Rimæ Daniell, an array of NNW-SSE-oriented grabens in Lacus Somniorum (Figs. 1C and 1D), indicate that these grabens are also located atop broad rises that stand 100–150 m above their surroundings (Fig. 2). The Rimæ Daniell grabens are comparable in width to those found in Schrödinger, but are only 50–100 m deep (Fig. 2). At both sites, evidence for fault-related flexure is not readily discernable with LOLA altimetry.

Ground displacements from slip events along faults can be simulated using the elastic dislocation program COULOMB (Lin and Stein, 2004; Toda et al., 2005). Utilizing the stress functions for an elastic half-space (Okada, 1992), and specifying fault plane geometries and fault offsets (see Fig. DR1), yields solutions for stresses and material displacements. As fault dips and offsets of the grabens can be directly measured from LOLA observations, they are the parameters that must be reproduced for the ground displacement models to be meaningful. After removing regional slopes of 0.5° to 1°, altimetric data can be compared with model results (Fig. 2) and statistically evaluated for goodness of fit (see the Data Repository). Simulated ground displacements utilizing measured fault dips and offsets from faults in Schrödinger basin and Rimæ Daniell both match LOLA topography proximal to the grabens, but do not recreate the broad topographic rises (Fig. 2).

## DIKE GROUND DISPLACEMENTS

Dikes—magma-filled, near-vertical opening-mode fractures at depth—cause characteristic ground displacements (Pollard et al., 1983; Mastin and Pollard, 1988) that can be accompanied by, and so have superposed fault-related surface displacements associated with, grabens directly above the intrusion (Rubin and Pollard, 1988; Rubin, 1992). Lunar grabens were previously suggested to be the surface expressions of dikes (Head and Wilson, 1993), e.g., at Rima Hyginus, where volcanic pits and pyroclastic deposits are collocated with grabens (Wilson et al., 2011). Similarly, grabens in Schrödinger basin are also superposed by vents with dark halos thought to represent pyroclastic units (Wilhelms et al., 1979; Fig. 1A), and volcanic vents are aligned in structural trends that follow the orientations of the grabens (Fig. 1B). No such relations are observed near the Rimæ Daniell grabens, however. Nonetheless, simulated ground displacements of dike intrusions alone satisfactorily recreate the long-wavelength topography around the grabens in both Rimæ Daniell and Schrödinger, although details of the grabens themselves are not well matched (Fig. 2).

If these grabens are underlain by dike intrusions, as observed on Earth (e.g., Rubin and Pollard, 1988; Rubin, 1992) and suggested for grabens on Mercury (Head et al., 2009), Venus (Ernst et al., 2003), the Moon (Head and Wilson, 1992), and Mars (e.g., Schultz et al., 2004), ground displacements from normal faulting should superpose the ground displacements from dike intrusions (Rubin and Pollard, 1988; Rubin, 1992). Indeed, simulated ground displacements for this scenario provide the best match to the LOLA profiles. In fact, the derived sample standard deviation between all LOLA topographic profiles and models of dike-related grabens is two to three times smaller than for models with grabens alone (Fig. 2). These findings indicate that the studied grabens are associated with, and potentially induced by, intrusive igneous activity.

## GEOMETRIC PROPERTIES OF DIKES

Large linear gravity anomalies hundreds of kilometers long and up to 25 km wide have been detected on the Moon by gravity gradiometry applied to observations by the Gravity Recovery and Interior Laboratory (GRAIL) (Zuber et al., 2013) at depths of 10–90 km. They are thought to be wide dikes that formed during the early global expansion of the Moon (Andrews-Hanna

<sup>1</sup>GSA Data Repository item 2014341, simulation details, statistical assessments, strength properties of the lunar lithosphere, and additional data on dike geometries, is available online at [www.geosociety.org/pubs/ft2014.htm](http://www.geosociety.org/pubs/ft2014.htm), or on request from [editing@geosociety.org](mailto:editing@geosociety.org) or Documents Secretary, GSA, P.O. Box 9140, Boulder, CO 80301, USA.

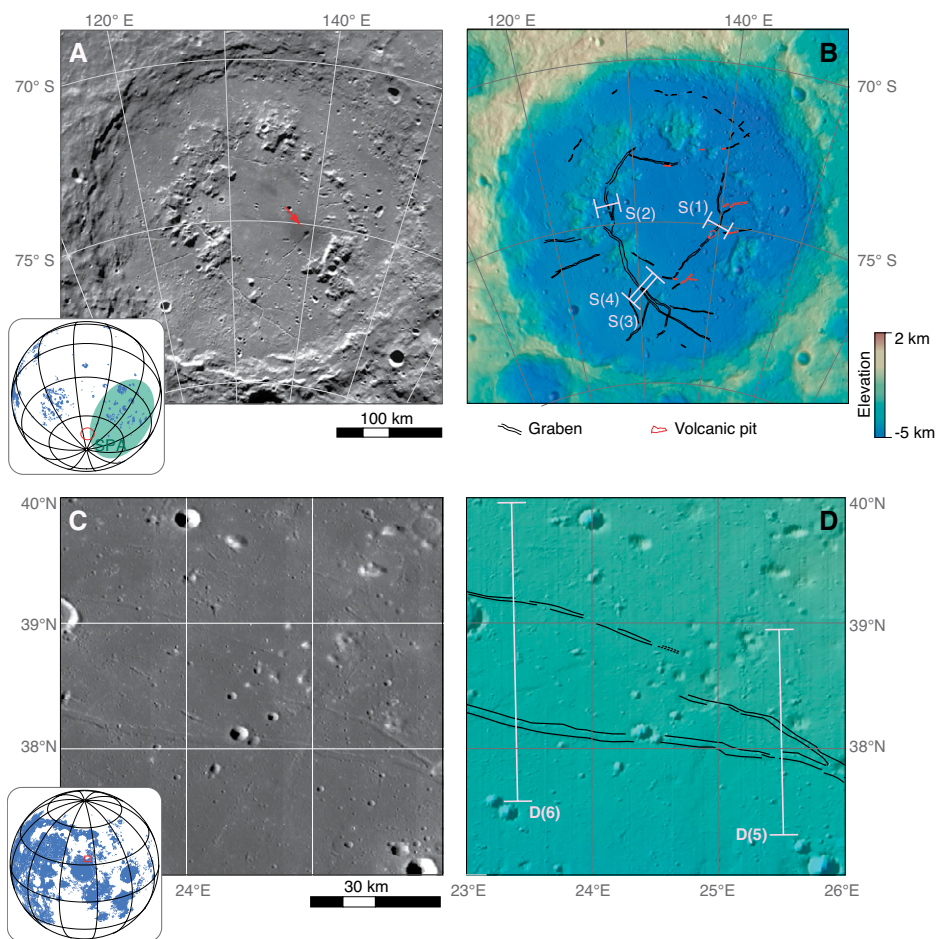


**Figure 1.** Grabens on the Moon analyzed in this study. **A:** Lunar Reconnaissance Orbiter-derived photogeologic mosaic of the 312-km-diameter Schrödinger basin located on the rim of the South Pole–Aitken basin (SPA), with its interior grabens clearly visible. Note the dark halo (red arrow) superposed on a graben near the eastern portion of the peak ring. **B:** Structural map superposed on color-coded Lunar Orbiter Laser Altimeter topography and shaded relief of Schrödinger basin. Pits (red outlines) follow the structural trends of the grabens. **C:** Photogeologic mosaic of the central portion of Rimæ Daniell. **D:** Structural map overlaid on color-coded topography and shaded relief of the central portion of Rimæ Daniell. Locations of topographic profiles (Fig. 2) are highlighted in B and D (start of each profile indicated by the location of the profile number). Maps have polar orthographic (A, B) and equirectangular (C, D) projections.

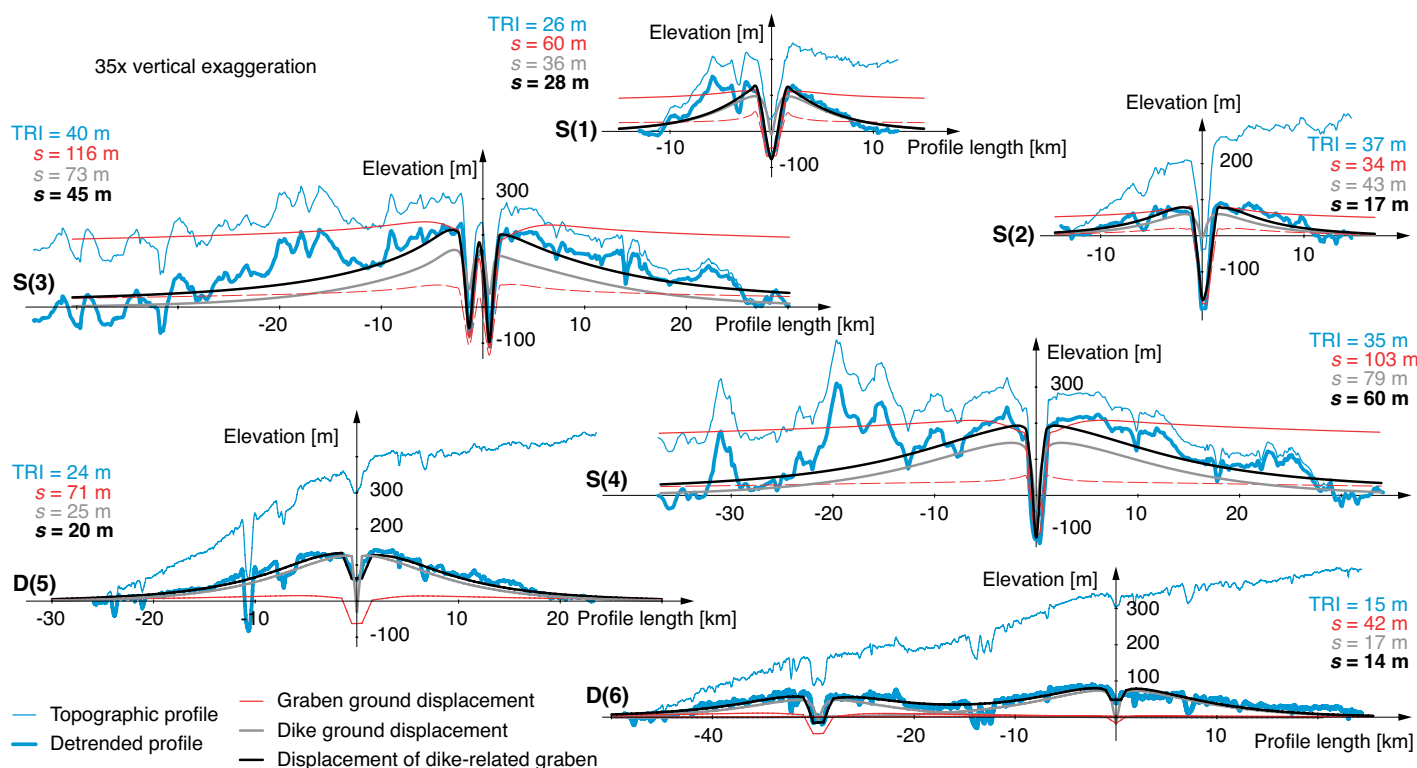


**Figure 2.** Observed and detrended topographic profiles (thin and thick blue lines, respectively) across lunar grabens in Schrödinger basin, S(1)–S(4), and Rimæ Daniell, D(5) and D(6). Simulated ground displacements of normal faults only (red lines), dikes (gray), and dikes with grabens (black) are shown. Terrain ruggedness index (TRI) and sample standard deviations (*s*) of simulated fits are given for each profile.

et al., 2013). Furthermore, the spatial correlation of long linear anomalies derived from Lunar Prospector magnetometer observations with mare ponds in the South Pole–Aitken basin (SPA) was taken as evidence for the presence of 25–50-km-wide zones of magnetized dikes that facilitated magma ascent and the formation of those mare ponds at 3.8–3.6 Ga (Purucker et al., 2012). Both analyses suggest that dikes and zones of dikes are present throughout the lunar lithosphere. However, none of the linear anomalies detected in one data set has been confirmed in the other, and no topographic expressions are associated with either of these types of linear anomaly. In addition, the spatial resolution of these data limits the detection of dikes to structures tens of kilometers in width.

The dike-related grabens identified in this study occur on much smaller scales. Therefore, topographic analysis of grabens with LOLA data is currently the only way to detect, and resolve the geometric properties of, stalled dikes. The depth below the surface to the top of the intrusion, together with its length ( $L$ ), height ( $H$ ), and aperture ( $a$ ) (Fig. 3), all of which are specified in the numerical setup, govern the shape of a dike's resulting topographic expression. A good fit between ground displacement models and LOLA topography, therefore, informs us of the geometric dimensions that lunar dikes may have. The derived sample standard deviations were used to assess the goodness of fit between models and observations. Only values equal to or less than the degree of ruggedness (as quantified by the terrain ruggedness index, TRI; Riley et al., 1999) of the analyzed terrain were considered satisfactory (see the Data Repository).

Although the results from this modeling approach are non-unique, only small ranges of intrusion geometries provide permissible sample standard deviations. Modeling results indi-

cate that dike length correlates with the length of the overlying graben, that the analyzed dikes are between 5 km and ~20 km in vertical extent, and that their maximum apertures range from 200 m to 500 m. Moreover, dikes are stalled at levels as shallow as 100–500 m below the surface.

## DISCUSSION

### Origin of Magmas

The largest dikes in the Schrödinger basin and Lacus Somniorum are detected at depths as deep as ~15–20 km. Crustal thickness values for these regions, derived from GRAIL data (Wieczorek et al., 2013), roughly coincide with these depth estimates, indicating that dikes extend to the lower crust. Pyroclastic deposits that superpose grabens show mafic spectral absorption features (Tompkins and Pieters, 2010), and impact-excavated mantle rocks (Wieczorek et al., 2013) are composed of olivine-rich materials (Yamamoto et al., 2010). Taken together, these observations imply that dike-forming magmas are of compositions similar to those of the lunar mantle, and so are potentially mantle derived.

Dike apertures are widely thought to be a function of magma rheology (e.g., Wada, 1994). In modern geologic settings, felsic, more viscous magmas are normally associated with wider dikes, whereas mafic magmas, with lower viscosities, produce dikes with apertures rarely exceeding a few meters. The widest dikes on Earth, however, occur as part of mafic dike swarms (Ernst et al., 2001) and have widths of up to 250 m, such as some olivine diabase dikes emplaced at 1.24 Ga as part of the Sudbury dike swarm (Canada) (Fahrig, 1987). Apertures of 200–500 m, as well as the inferred depth extents and compositions, for the lunar structures analyzed here com-

pare well with those of structures previously hypothesized for the Moon (Head and Wilson 1992, 1993) and with those of some individual dikes of the Sudbury and other Proterozoic dike swarms on Earth. This suggests that dike width as a function of magma rheology is only a secondary phenomenon. Emplacement conditions (e.g., increased magma pressures [Wada, 1994] and thermal erosion of surrounding rocks [Fialko and Rubin, 1999]), tectonic settings (Fialko and Rubin, 1999), and strength properties of the host rock (Krumbholz et al., 2014) therefore play a greater role.

### Implications for Lunar Tectonics

Dike widening by thermal erosion of the surrounding rock may have occurred on the Moon, but this process does not contribute to the accumulation of ground displacements and thus cannot be assessed with an analysis of topography. However, the geometries of dikes may be related to magma overpressures (Rubin, 1995), serving as a test of the plausibility of the modeling results and providing clues to rock strength properties and tectonic regimes present within the lunar lithosphere during dike emplacement (see details in the Data Repository). For a tectonically neutral regime (where stresses are dominated by the overburden pressure only) with a lithosphere that is moderately weakened by impact events, inferred magma overpressures for 10 identified dikes (see the Data Repository) range from 50 to 330 MPa, with the median value at ~110 MPa (Fig. 3).

These values greatly exceed the tensile strength of a moderately fractured lunar lithosphere, suggesting that dikes as large as those in this study may be accompanied by sizeable secondary fractures and damage zones. Magma overpressures required to form dikes with the geometries derived here would be substantially lower if the lithosphere were under extension or were weakened by an even higher degree of fracturing and brecciation from impact bombardment. Indeed, the bulk density of the lunar crust is lower than previously thought, a finding attributed to higher porosities caused by impact events (Wieczorek et al., 2013).

The dikes in this study occur in several geologic settings, for which several sources of extensional stresses may be invoked. Tectonic activity inside Schrödinger basin may be linked to post-impact uplift and viscous relaxation (Solomon and Comer, 1982), which produced extensional stresses that may have facilitated dike intrusion there. The Rimæ Daniell dikes occur partly concentric to Mare Serenitatis, a large mascon basin. Extensional stresses here may originate from cooling of the mare units, as has been proposed for buried basins and craters in Mercury's northern volcanic plains (Freed et al., 2012), from mascon loading (Freed et al., 2001), or from both processes.

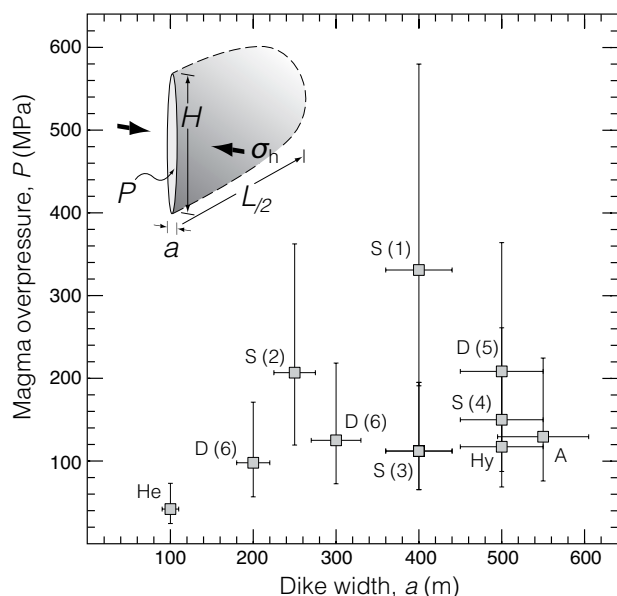


**Figure 3. Magma overpressures ( $P$ ) within dikes of height  $H$  and length  $L$  shown as a function of dike aperture ( $a$ ). Values for  $P$  are given for a neutral tectonic regime, in which all acting stresses ( $\sigma_h$ ) are equal to the overburden pressure. Error bars in the y-direction indicate variations in host-rock strength properties for a moderately (upper bar) to highly (lower bar) fractured lithosphere. Error bars in the x-direction assume 5% uncertainty. D—Rimæ Daniell; S—Schrödinger basin; He—Rima Hesiodus; Hy—Rima Hyginus; A—Rima Ariadaeus.**

## CONCLUSIONS

Topographic characteristics of many of the large lunar graben systems cannot be solely explained by normal faulting. Their long-wave-length morphologies much more likely originate from the opening of dikes at depth. Ground displacement simulations reveal that the observed topography proximal to these grabens is due to dikes wider than 100 m that likely penetrate the lunar crust down to depths of ~20 km. Such geometric properties require a regionally extensional tectonic regime and a moderately to heavily fractured lunar lithosphere during dike emplacement. These results give insight into the nature and geometry of lunar magmatic systems in particular, and provide a basis for further understanding the interplay between lunar magmatism and tectonics in general.

## ACKNOWLEDGMENTS

I thank Paul K. Byrne and Shoshana Z. Weider for discussions and their editorial eye. The insightful comments from L. Wilson, R.E. Ernst, and a third, anonymous reviewer are greatly acknowledged. This research made use of NASA's Planetary Data System and Astrophysics Data System.

## REFERENCES CITED

- Andrews-Hanna, J.C., et al., 2013, Ancient igneous intrusions and early expansion of the Moon revealed by GRAIL gravity gradiometry: *Science*, v. 339, p. 675–678, doi:10.1126/science.1231753.
- Ernst, R.E., Grosfils, E.B., and Mège, D., 2001, Giant dike swarms: Earth, Venus and Mars: *Annual Review of Earth and Planetary Sciences*, v. 29, p. 489–534, doi:10.1146/annurev.earth.29.1.489.
- Ernst, R.E., Desnoyers, D.W., Head, J.W., and Grosfils, E.B., 2003, Graben-fissure systems in Guinevere Planitia and Beta Regio (264°312'E, 24°60'N), Venus, and implications for regional stratigraphy and mantle plumes: *Icarus*, v. 164, p. 282–316, doi:10.1016/S0019-1035(03)00126-X.
- Fahrig, W.F., 1987, The tectonic setting of continental mafic dyke swarms: Failed arm and early passive margin, in Halls, H.C. and Fahrig, W.F., eds., *Mafic Dyke Swarms: Geological Association of Canada Special Publication 34*, p. 331–348.
- Fialko, Y.A., and Rubin, A.M., 1999, Thermal and mechanical aspects of magma emplacement in giant dike swarms: *Journal of Geophysical Research*, v. 104, p. 23,033–23,049, doi:10.1029/1999JB900213.
- Freed, A.M., Melosh, H.J., and Solomon, S.C., 2001, Tectonics of mascon loading: Resolution of the strike-slip faulting paradox: *Journal of Geophysical Research*, v. 106, p. 20,603–20,620, doi:10.1029/2000JE001347.
- Freed, A.M., Blair, D.M., Watters, T.R., Klimczak, C., Byrne, P.K., Solomon, S.C., Zuber, M.T., and Melosh, H.J., 2012, On the origin of graben and ridges within and near volcanically buried craters and basins in Mercury's northern plains: *Journal of Geophysical Research*, v. 117, E00L06, doi:10.1029/2012JE004119.
- Head, J.W., and Wilson, L., 1992, Lunar mare volcanism: Stratigraphy, eruption conditions, and the evolution of secondary crusts: *Geochimica et Cosmochimica Acta*, v. 56, p. 2155–2175, doi:10.1016/0016-7037(92)90183-J.
- Head, J.W., and Wilson, L., 1993, Lunar graben formation due to near-surface deformation accompanying dike emplacement: *Planetary and Space Science*, v. 41, p. 719–727, doi:10.1016/0032-0633(93)90114-H.
- Head, J.W., et al., 2009, Evidence for intrusive activity on Mercury from the first MESSENGER flyby: *Earth and Planetary Science Letters*, v. 285, p. 251–262, doi:10.1016/j.epsl.2009.03.008.
- Krumbholz, M., Hieronymus, C.F., Burchardt, S., Troll, V.R., Tanner, D.C., and Friese, N., 2014, Weibull-distributed dyke thickness reflects probabilistic character of host-rock strength: *Nature Communications*, v. 5, 3272, doi:10.1038/ncomms4272.
- Lin, J., and Stein, R.S., 2004, Stress triggering in thrust and subduction earthquakes, and stress interaction between the southern San Andreas and nearby thrust and strike-slip faults: *Journal of Geophysical Research*, v. 109, B02303, doi:10.1029/2003JB002607.
- Mastin, L.G., and Pollard, D.D., 1988, Surface deformation and shallow dike intrusion processes at Inyo Craters, Long Valley, California: *Journal of Geophysical Research*, v. 93, p. 13,221–13,235, doi:10.1029/JB093iB11p13221.
- Okada, Y., 1992, Internal deformation due to shear and tensile faults in a half-space: *Bulletin of the Seismological Society of America*, v. 82, p. 1018–1040.
- Pollard, D.D., Delaney, P.T., Duffield, W.A., Endo, E.T., and Okamura, A.T., 1983, Surface deformation in volcanic rift zones: *Tectonophysics*, v. 94, p. 541–584, doi:10.1016/0040-1951(83)90034-3.
- Purucker, M.E., Head, J.W., and Wilson, L., 2012, Magnetic signature of the lunar South Pole-Aitken basin: Character, origin, and age: *Journal of Geophysical Research*, v. 117, E05001, doi:10.1029/2011JE003922.
- Riley, S.J., DeGloria, S.D., and Elliot, R., 1999, A terrain ruggedness index that quantifies topographic heterogeneity: *Intermountain Journal of Sciences*, v. 5, p. 23–27.
- Rubin, A.M., 1992, Dike-induced faulting and graben subsidence in volcanic rift zones: *Journal of Geophysical Research*, v. 97, p. 1839–1858, doi:10.1029/91JB02170.
- Rubin, A.M., 1995, Propagation of magma-filled cracks: *Annual Review of Earth and Planetary Sciences*, v. 23, p. 287–336, doi:10.1146/annurev.earth.23.050195.001443.
- Rubin, A.M., and Pollard, D.D., 1988, Dike-induced faulting in rift zones of Iceland and Afar: *Geology*, v. 16, p. 413–417, doi:10.1130/0091-7613(1988)016<0413:DIFIRZ>2.3.CO;2.
- Schultz, P.H., 1976, Floor-fractured lunar craters: *The Moon*, v. 15, p. 241–273, doi:10.1007/BF00562240.
- Schultz, R.A., Okubo, C.H., Goudy, C.L., and Wilkins, S.J., 2004, Igneous dikes on Mars revealed by Mars Orbiter Laser Altimeter topography: *Geology*, v. 32, p. 889–892, doi:10.1130/G20548.1.
- Schultz, R.A., Soliva, R., Okubo, C.H., and Mège, D., 2010, Fault populations, in Watters, T.R., and Schultz, R.A., eds., *Planetary Tectonics: Cambridge, UK, Cambridge University Press*, p. 457–510.
- Smith, D.E., et al., 2010, The Lunar Orbiter Laser Altimeter investigation on the Lunar Reconnaissance Orbiter Mission: *Space Science Reviews*, v. 150, p. 209–241, doi:10.1007/s11214-009-9512-y.
- Solomon, S.C., and Comer, R.P., 1982, The evolution of impact basins: Viscous relaxation of topographic relief: *Journal of Geophysical Research*, v. 87, p. 3975–3992, doi:10.1029/JB087iB05p3975.
- Toda, S., Stein, R.S., Richards-Dinger, K., and Bozkurt, S., 2005, Forecasting the evolution of seismicity in southern California: Animations built on earthquake stress transfer: *Journal of Geophysical Research*, v. 110, B05S16, doi:10.1029/2004JB003415.
- Tompkins, S., and Pieters, C.M., 2010, Spectral characteristics of lunar impact melts and inferred mineralogy: *Meteoritics & Planetary Science*, v. 45, p. 1152–1169, doi:10.1111/j.1945-5100.2010.01074.x.
- Wada, Y., 1994, On the relationship between dike width and magma viscosity: *Journal of Geophysical Research*, v. 99, p. 17,743–17,755, doi:10.1029/94JB00929.
- Watters, T.R., and Johnson, C.L., 2010, Lunar tectonics, in Watters, T.R., and Schultz, R.A., eds., *Planetary Tectonics: Cambridge, UK, Cambridge University Press*, p. 121–182.
- Wieczorek, M.A., et al., 2013, The crust of the Moon as seen by GRAIL: *Science*, v. 339, p. 671–675, doi:10.1126/science.1231530.
- Wilhelms, D., Howard, K., and Wilshire, H., 1979, *Geologic map of the south side of the Moon: U.S. Geological Survey Miscellaneous Investigations Series Map I-1162*, scale 1:5,000,000.
- Wilson, L., Hawke, B.R., Giguere, T.A., and Petrycki, E.R., 2011, An igneous origin for Rima Hyginus and Hyginus crater on the Moon: *Icarus*, v. 215, p. 584–595, doi:10.1016/j.icarus.2011.07.003.
- Yamamoto, S., et al., 2010, Possible mantle origin of olivine around lunar impact basins detected by SELENE: *Nature Geoscience*, v. 3, p. 533–536, doi:10.1038/ngeo897.
- Zuber, M.T., Smith, D.E., Lehman, D.H., Hoffman, T.L., Asmar, S.W., and Watkins, M.M., 2013, Gravity Recovery and Interior Laboratory (GRAIL): Mapping the lunar interior from crust to core: *Space Science Reviews*, v. 178, p. 3–24, doi:10.1007/s11214-012-9952-7.

Manuscript received 16 June 2014

Revised manuscript received 8 August 2014

Manuscript accepted 9 August 2014

Printed in USA



# **GSA DATA REPOSITORY 2014341**

**Supplement to:**

## **Geomorphology of Lunar Grabens Requires Igneous Dikes at Depth**

**Christian Klimczak**

### **TOPOGRAPHIC PROFILES AND NUMERICAL SIMULATIONS**

#### **Topographic data used and rationale for analyzed grabens**

Topographic profiles in Schrödinger basin (profiles 1 to 4) were extracted from the gridded 1024 ppd LOLA product ([http://imbrium.mit.edu/BROWSE/LOLA\\_GDR/CYLINDRICAL.html](http://imbrium.mit.edu/BROWSE/LOLA_GDR/CYLINDRICAL.html)), and topographic measurements from individual LOLA tracks were extracted from the Lunar Orbital Data Explorer (<http://ode.rsl.wustl.edu/moon/indextools.aspx>) for Rimæ Daniell (profiles D5 and D6) and other ~E-W oriented graben structures (see below). Original profiles show a 0.5° to 1° slope (Figure 2, thin blue line), that is shown with 35 times exaggeration in all profiles. Linear slopes were obtained from the relationship between the topographic difference and the horizontal distance of the first to the last data point in the extracted profile. All profiles were then detrended by removing the linear slope (Figure 2, thick blue line) to allow for better comparison to ground displacement simulations.

In the polar regions (e.g., examples for Schrödinger basin), LOLA coverage is dense so that the gridded LOLA product is of sufficient resolution for topographic profiles across grabens to be extracted and analyzed without too many interpolation artifacts. The gridded product is of insufficient resolution in the mid-latitudes and equatorial regions, as too many interpolation artifacts affect topographic profiles, especially if they are taken in the N–S direction. Individual LOLA tracks, which are oriented N–S due to the polar orbit of the Lunar Reconnaissance Orbiter (LRO) spacecraft, are required for an analysis instead. This then limits an analysis to more or less E–W oriented grabens in these regions.

The analysis of lunar grabens in this study was also limited to only the most prominent structures (widest and deepest troughs) that meet criteria for data coverage and data resolution (see above). All suitable examples were topographically evaluated. They occur in various geologic settings (edge of mascon basins, periphery of maria, on the floors of impact basins) and across the entire lunar surface (northern mid-latitudes, equator, southern mid-latitudes, and south polar region) so that this study can be considered planet-wide. Planet-wide, all grabens suited for the analysis have the potential to be underlain by a dike.

#### **Sample standard deviations between the topographic profiles and simulations**

Ground displacements were simulated using the open-source code COULOMB (Lin and Stein, 2004; Toda et al., 2005) run in MatLab®, by specifying and varying geometric properties of a graben alone (Figure DR1A), dike alone, and dike–gaben combination (Figure DR1B) until a visually good fit is obtained. Good fits to topographic

profiles are only achieved for a narrow range of geometric properties, giving confidence that simulated structures are good approximations of structures present on the Moon.

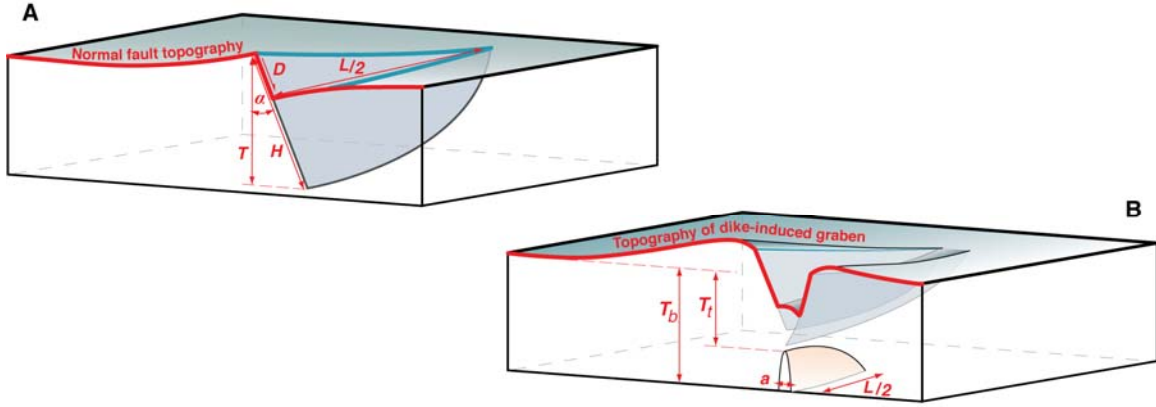


**Figure DR1.** Stylized geomorphology of planetary graben settings. A) Planetary half-graben geomorphology is comprised of a gentle synclinal flexure in the rock units below the fault plane (i.e., foot wall syncline) as well as a gentle anticlinal flexure in the rock units above the fault plane (i.e., hanging wall anticline). Topographic extent and range of the landform, as well as degree of flexure of rock units are governed by the fault geometry, including fault length ( $L$ ), fault height ( $H$ ), fault displacement ( $D$ ), fault dip ( $\alpha$ ) and depth of faulting ( $T$ ). B) Dike-related graben geomorphology is governed by normal fault geometric properties as well as geometry of the underlying dike. The dike geometry is characterized by dike width or aperture ( $a$ ), dike length ( $L$ ), and depth below surface to the top ( $T_t$ ) and approximate bottom ( $T_b$ ) of the dike. The difference between  $T_t$  and  $T_b$  equates to the height,  $H$ , of the dike.

To assess the goodness of fit between the topography and the simulated ground displacements, a standard sample deviation ( $s$ ) was calculated. The sample standard deviation is given as:

$$s = \sqrt{\frac{1}{N-1} \sum_{i=1}^N (x_i - \bar{x})^2}, \quad (1)$$

where  $N$  is the total number of simulated data points. The term  $(x_i - \bar{x})$  represents the residuals between simulation and observation, with  $x_i$  being the  $i^{\text{th}}$  data point of the simulation, and  $\bar{x}$  being the topographic value at the  $i^{\text{th}}$  datapoint that is tried to be matched with  $x_i$ . Values of  $s$  provide a measure of the average deviation of simulated ground displacements from the topography, and thus simulations with a lower  $s$  have a better fit. Residuals for profile S(4) (Figure 2) are given as example (Figure DR2). Residuals for the graben fit are small at or near the graben but become larger further away from the structure. In general, dike and dike-related graben fits have much lower residuals throughout the entire profile. However, the ruggedness of the topography affects sample standard deviations, showing that more rugged topographies cannot be as accurately recreated by numerical models as topographically smoother areas (Figure 2),

and thus it is difficult to compare the goodness of fit for simulated ground displacements between different profiles with the sample standard deviations alone.

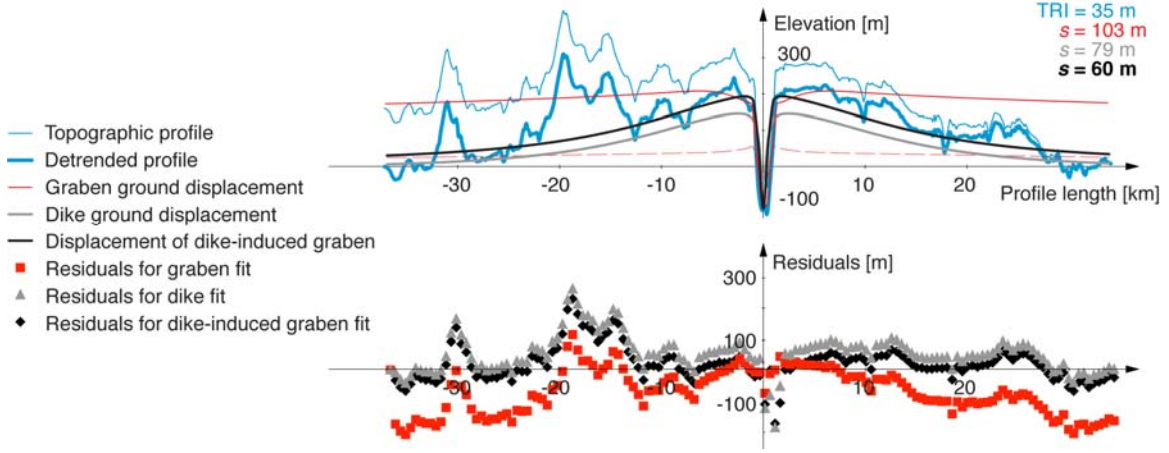


**Figure DR2.** Ground displacement simulations and topography for profile S(4) (top) and corresponding residuals between the models and observed topography (bottom). Note that the residuals are highest in the topographically most rugged portion of the profile.

### Two-dimensional Topographic Ruggedness Index (TRI)

The topographic ruggedness index (TRI) is a measure of the average amount of elevation difference between adjacent topographic measurements in a digital elevation model (Riley et al., 1999). For three-dimensional datasets, the TRI is the average of the absolute values of the elevation difference from a center cell and the eight cells immediately surrounding it. For two-dimensional elevation data (i.e., topographic profiles), this algorithm was modified to solve for the average of the absolute values of the elevation difference of the neighboring data points, expressed as:

$$TRI = \sqrt{\frac{1}{N} \sum_{i=1}^N (x_i - x_{i+1})^2}. \quad (2)$$

Here,  $N$  is the total number of topographic measurements,  $x_i$  is the  $i^{\text{th}}$  topographic measurement of the profile, and  $x_{i+1}$  is the topographic measurement neighboring  $x_i$ . As the TRI value defines the average change of elevation between measurements within the topographic profile, the  $s$  values should not exceed the TRI values for a simulated fit to be considered as “good”, as sample standard deviations of the models are then smaller than the average natural variation in the observational data. This rule allows for larger sample standard deviations in more rugged terrains and demands smaller sample standard deviations in smoother terrains, thus enabling comparison of goodness of fits between different types of terrain.

Elevation differences between neighboring measurements are again given for profile S(4) as example (Figure DR3). Generally, the changes in elevation between neighboring measurements over the entire profile are rather low, mostly below 10 m and

in the more rugged regions between 20 and 40 m. The graben at the origin of the diagram is the most rugged landform of the entire topographic profile with 150 m change between measurements. The left portion of the profile is more rugged than the right portion, caused by rough hummocky basin floor material (Kramer et al., 2013). Therefore, the residuals between the models and observed topography are larger in the left portion than the right one (Figure DR2). The TRI value of this profile is 35 m. This value almost twice as low as the  $s$  value for the best-fit simulation of a dike-related graben. Generally, however, the residuals for this fit are quite low, especially on the right portion of the profile, where there is no rough geologic surface unit.

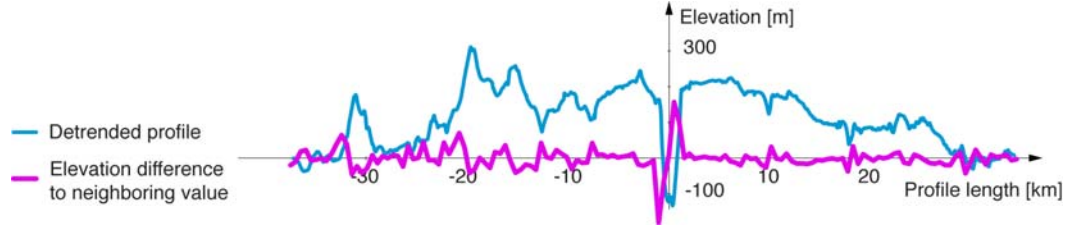


**Figure DR3.** Topographic profile S(4) and elevation difference of the neighboring data points.

## ELASTIC PROPERTIES OF A FRACTURED LUNAR LITHOSPHERE

The lunar lithosphere very likely consists of a combination of intact rock and associated structural weaknesses, such as fractures, impact damage zones, and lithologic contacts that together weaken the overall material. The rock mass rating (RMR) system, measured on a scale from 0 to 100, where 100 represents intact rock, is frequently used in geo-engineering and geomechanics applications to account for the degree and condition of weaknesses (as well as for pore pressure conditions) within a rock (Bieniawski, 1989) to better evaluate elastic rock properties on lithospheric scales (Schultz, 1993, 1995, 1996).

Elastic rock properties include Young's Modulus,  $E$ , and the related Shear Modulus ( $\mu$ ). Either one of these properties is required to calculate magma overpressures ( $P$ ) within a dike (Figure 3) using the relation (Rubin, 1995):

$$a = \frac{(P - \sigma_h)}{\mu/(1 - \nu)} 1/2 H, \quad (3)$$

with  $\nu$  being Poisson's Ratio and  $\sigma_h$  being the surrounding stress. In a neutral tectonic regime, this stress is equal to the confining pressure (overburden). Young's Modulus and the Shear Modulus depend on confining pressure that increases with depth,  $z$ . For conditions appropriate for Earth this is estimated as (Schultz et al., 2006):

$$E = E^* + z^{0.4}, \quad (4)$$

where  $E^*$  denotes the Deformation Modulus. Empirical studies found that  $E^*$  is relatively insensitive to rock type, and that it relates to RMR as:



$$E^* = 2 \text{ RMR} - 100 \quad \text{for RMR} > 50 \quad (5a)$$

and

$$E^* = 10^{(\text{RMR} - 10)/40} \quad \text{for RMR} < 50, \quad (5b)$$

with the units of  $E^*$  given in GPa (Bieniawski, 1989). Deformation Moduli for rock masses of moderate quality (RMR 55) are ~10 GPa, Deformation Moduli of rock masses of poor quality (RMR 35 to 45), such as expected for the heavily fractured upper lunar lithosphere (Wieczorek et al., 2013), are 4.2 to 7.5 GPa.

The depth dependent Deformation Modulus (Eq. 4) on other rocky bodies is then obtained by using a scaling relation (Schultz et al., 2006) given as:

$$E = E^* \left( \frac{g}{g_{\text{Earth}}} \right) \left( \frac{\rho}{\rho_{\text{Earth}}} \right) z^{0.4}, \quad (6)$$

where the term  $\left( \frac{g}{g_{\text{Earth}}} \right)$  is the normalized surface gravitational acceleration and the term  $\left( \frac{\rho}{\rho_{\text{Earth}}} \right)$  is the normalized rock density (see details in Schultz et al., 2006). The depth dependent Deformation Modulus for conditions appropriate on the Moon ( $g = 1.6 \text{ m/s}^2$  and bulk density of the upper lithosphere of  $\rho \approx 2600 \text{ kg/m}^3$  (Wieczorek et al., 2013)) can now be used to calculate magma overpressures (Eq. 3), if dike geometric properties ( $a$ ,  $H$ ) and surrounding stresses are known.

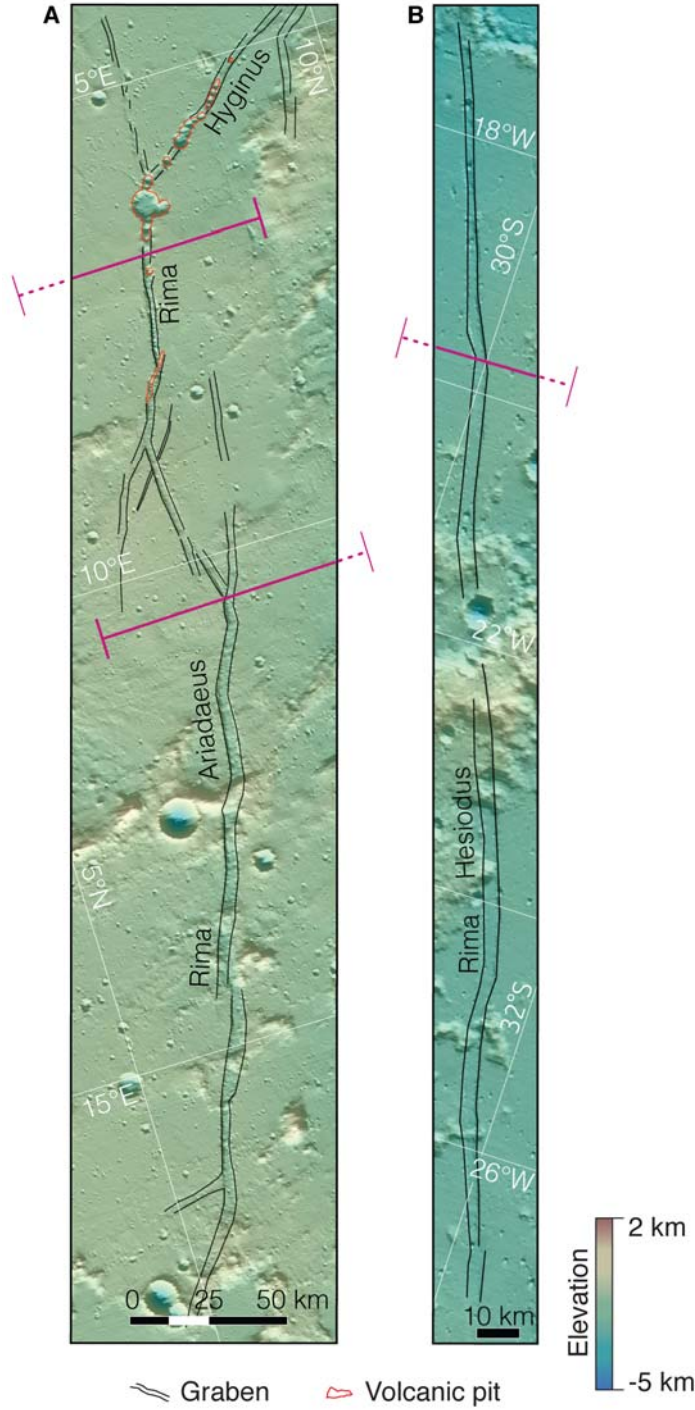
## DIKE GEOMETRIES

Magma overpressures (Eq.3) were estimated for 10 dikes. Dike dimensions were inferred from ground displacement modeling of four structures inside Schrödinger basin (Figure 2), as well as from three structures along two profiles across Rimæ Daniell (Figure 2) and for Rima Ariadaeus, Rima Hyginus, and Rima Hesiodus (Figure DR4). Ground displacement fits for the latter three structures are presented in Figure DR5. Rima Ariadaeus is a topographically very pronounced and asymmetric graben. Rima Hyginus is also a topographically prominent graben structure. Both grabens show a structural relief of up to 450 m and lie on a topographic rise (Figure DR5), similar to grabens in Schrödinger basin. In addition, Rima Hyginus displays a series of volcanic pits and volcanic deposits following the structural trend of the graben (Wilson et al., 2011; Figure DR4). Both topographic profiles are best approximated with the ground displacements of a dike-related graben.

Rima Hesiodus is a ~280-km-long graben structure cutting through highlands and mare units (Figure DR4). Its structural relief of only 100 to 120 m is smaller than that of other lunar grabens of similar length. Modeled ground displacements of a graben alone

and a dike-related graben are equally good (Figure DR5), thus indicating that a dike could be present at depth but may not be invoked for this particular structure.

All potential dike-related grabens of this study, including the derived best-fit dike geometric properties are listed in Table DR1.



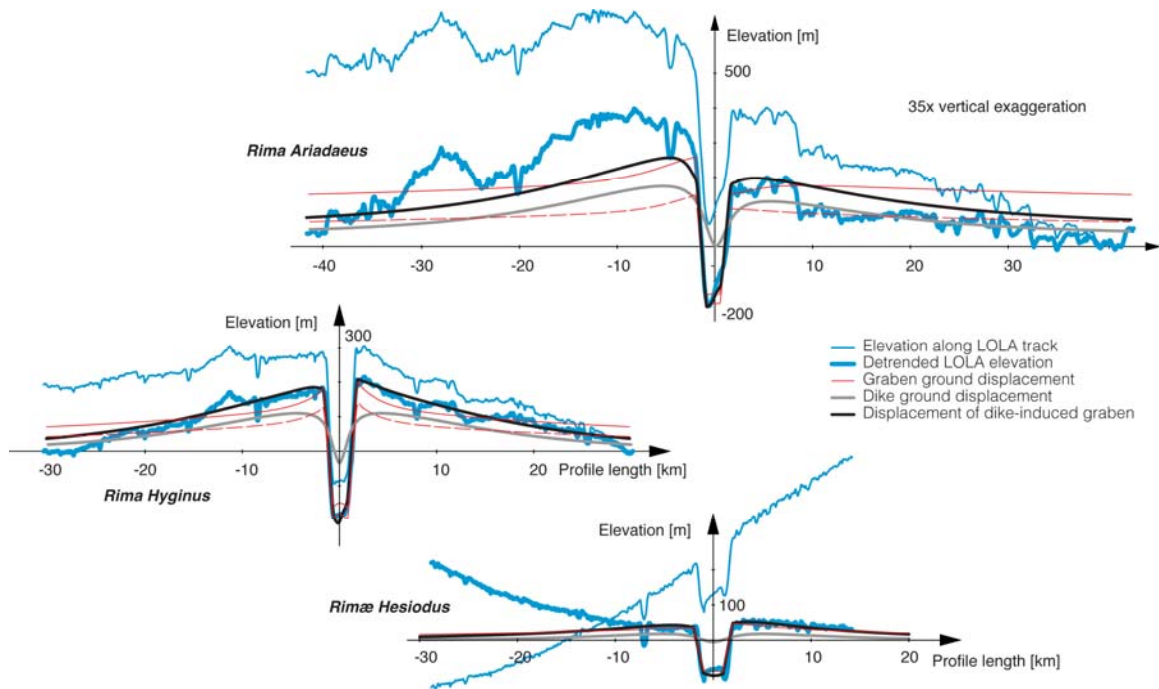


**Figure DR5.** Observed and detrended LOLA profiles (blue) across Rima Ariadaeus (from S to N), Rima Hyginus (S to N), and Rima Hesiodus (N to S) with simulated ground displacements of normal faults only (red) dikes (grey) and dike-related grabens (black). Rima Ariadaeus and Rima Hyginus are best matched with the ground displacement of a dike-related graben. Ground displacements of both graben alone and dike-related graben match the topography across Rima Hesiodus equally well.

**Table DR1.** Table of dike geometric properties derived from ground displacement simulations matched to LOLA topographic profiles.

Structure	Dike aperture, $a$	Depth to top of dike, $T_t$	Approximate depth to bottom of dike, $T_b$	Dike height, $H$
Schrödinger S(1)	400	0.5	5.5	5
Schrödinger S(2)	250	0.5	5.5	5
Schrödinger S(3)	400	0.3	15.3	15
Schrödinger S(3)	400	0.3	15.3	15
Schrödinger S(4)	500	0.3	14.3	14
Rima Daniell D(5)	500	0.1	10.1	10
Rima Daniell D(6)	200	0.35	8.85	8.5
Rima Daniell D(6)	300	0.3	10.3	10
Rima Ariadaeus A	550	2.5	20.5	18
Rima Hyginus Hy	500	1	19	18
Rima Hesiodus He	100	2	12	10

## REFERENCES CITED

- Bieniawski, Z.T., 1989, Engineering rock mass classifications: New York, Wiley.
- Kramer, G.Y., Kring, D.A., Nahm, A.L., Pieters, C.M., 2013, Spectral and photogeologic mapping of Schrödinger Basin and implications for post-South Pole-Aitken impact deep subsurface stratigraphy: *Icarus*, v. 223, p. 131–148, doi: 10.1016/j.icarus.2012.11.008.
- Lin, J., and Stein, R.S., 2004, Stress triggering in thrust and subduction earthquakes, and stress interaction between the southern San Andreas and nearby thrust and strike-slip faults: *Journal of Geophysical Research*, v. 109, B02303, doi:10.1029/2003JB002607.
- Riley, S. J., DeGloria, S.D., and Elliot, R., 1999, A terrain ruggedness index that quantifies topographic heterogeneity: *Intermountain Journal of Sciences*, v. 5, no. 1–4, p. 23–27.
- Schultz, R.A., 1993, Brittle strength of basaltic rock masses with applications to Venus: *Journal of Geophysical Research*, v. 98, p. 10883–10895.
- Schultz, R.A., 1995, Limits on strength and deformation properties of jointed basaltic rock masses: *Rock Mechanics and Rock Engineering*, v. 28, p. 1–15.
- Schultz, R.A., 1996, Relative scale and the strength and deformability of rock masses: *Journal of Structural Geology*, v. 18, p. 1139–1149.
- Schultz, R.A., Okubo, C.H., Wilkins, S., 2006, Displacement-length scaling relations for faults on the terrestrial planets: *Journal of Structural Geology*, v. 28, p. 2182–2193.
- Toda, S., Stein, R.S., Richards-Dinger, K., and Bozkurt, S., 2005, Forecasting the evolution of seismicity in southern California: Animations built on earthquake stress transfer: *Journal of Geophysical Research*, v. 110, B05S16, doi:10.1029/2004JB003415.
- Wieczorek, M.A., and 15 other, 2013, The Crust of the Moon as Seen by GRAIL: *Science*, v. 339, no. 6120, p. 671–674, doi:10.1126/science.1231530.
- Wilson, L., Hawke, B.R., Giguere, T.A., Petrycki, E.R., 2011, An igneous origin for Rima Hyginus and Hyginus crater on the Moon: *Icarus*, v. 215, no. 2, p. 584–595.